



Characteristics and Control Measures of Deep and Shallow Dense Drilling in Roadway for Pressure Relieving by Cutting Roof

Xiaoming Sun^{1,2} · Zhenmin Qi^{1,2} · Yong Zhang^{1,2} · Zhihu Li^{1,2} · Cheng Xie^{1,2} · Jinkun Yang^{1,2} · Jiaxu Ding^{1,2} · Linsen He^{1,2}

Received: 3 November 2023 / Accepted: 11 February 2024 / Published online: 2 March 2024
© Society for Mining, Metallurgy & Exploration Inc. 2024

Abstract

To solve the problem of large deformation of deep soft rock roadway, taking the soft rock roadway of no. 1 coal mine in New Shanghai as an engineering example, the deformation mechanism of surrounding rock of deep soft rock roadway is analyzed by combining theoretical analysis, numerical simulation and field test, and the control countermeasures centering on deep and shallow dense drilling are put forward. Through theoretical derivation, based on the masonry beam theory, surrounding rock structure S-R stability principle and composite beam principle, the length, angle, and spacing of deep and shallow dense drilling are determined. Through numerical simulation, the deformation evolution process of soft rock roadway surrounding rock after dense drilling pressure relief is reproduced, and the influence of drilling parameters (drilling spacing, dip angle) on pressure relief effect is analyzed and compared. The field application test and monitoring verify that the deformation control measures of deep and shallow dense drilling broken roof surrounding rock have a good effect of large deformation control of soft rock roadway, and provide a new support means for the safety and stability control of soft rock roadway.

Keywords Deep · Soft rock · Large deformation of roadway · Deep and shallow dense boreholes

1 Introduction

With the increasing complexity of coal mining conditions, the issue of controlling weak roof and floor in the tunnels has become more prominent. Problems such as significant deformation and severe fragmentation of the roof and floor, frequent occurrences of roof and floor bumps, and difficulties in supporting and maintaining have been widely observed [1–4]. These issues significantly constrain the safe and efficient exploitation of deep coal resources.

One effective method for controlling the stability of deep tunnels is through tunnel destressing [5]. Researchers from

around the world have conducted extensive studies on in-tunnel destressing techniques, such as slotting [6], drilling [7], and loosening blasting [8], as well as out-tunnel destressing techniques, such as destressing galleries [9] and extraction layer mining [10]. In particular, in-tunnel destressing techniques weaken the local load-bearing capacity of the surrounding rock and transfer high stresses from the tunnel perimeter, ensuring tunnel stability.

Common in-tunnel destressing techniques in coal mines include hydraulic fracturing, deep-hole blasting, and dense drilling. Among these, dense drilling, which weakens the immediate roof, is known for its high safety, low cost, and adaptability. Numerous scholars have extensively studied drilling destressing techniques. Yi Enbing et al. [11], for instance, conducted an analysis of the effects of large-diameter drilling destressing on both soft and hard coal seams. They concluded that drilling destressing is more effective in soft coal seams compared to hard coal seams. Liu Honggang et al. [12] proposed that a well-arranged destressing borehole can structurally pre-fracture the surrounding rock of the tunnel, causing high-stress rock to transfer to deeper layers. Zhang et al. [13] researched the development of local fractures around the boreholes and found that a higher borehole density

✉ Yong Zhang
zhangyong_198989@126.com

Zhenmin Qi
cumtbqzm@163.com

¹ State Key Laboratory for Geomechanics and Deep Underground Engineering, China University of Mining and Technology (Beijing), Beijing 100083, China

² School of Mechanics and Civil Engineering, China University of Mining and Technology (Beijing), Beijing 100083, China

results in more developed fractures and better destressing effects. Jia Chuanyang et al. [14] suggested that stress release due to crack propagation is the fundamental reason for the destressing effect of drilling boreholes. Moreover, the larger the borehole diameter, the greater the borehole depth, and the smaller the spacing between boreholes, the better the destressing effect. Wang Meng et al. [15] categorized the degree of destressing into three types: insufficient destressing, sufficient destressing, and excessive destressing. They studied the dynamic effects of destressing borehole length, diameter, and spacing on the stability of deep tunnel surrounding rock. Liu Huabo et al. [16] analyzed the distribution characteristics of support pressure in front of the working face, confirming the weakening effect of large-diameter destressing boreholes on working face support pressure. Gai Decheng et al. [17] investigated the displacement field, stress field, plastic zone, elastic energy density, and local energy release rate of coal bodies subjected to drilling destressing under high-stress conditions. They proposed a theoretical framework for applying different borehole spacing in different strength coal bodies. The above-mentioned studies have explored the mechanics of drilling destressing. However, there is limited literature on the mechanisms of deep and shallow dense drilling destressing and their effects on tunnel stability.

This paper is conducted against the backdrop of the deep and shallow dense borehole pressure relief tunnel at the New Shanghai No.1 Coal Mine. It employs a combination of theoretical analysis, numerical simulation, and industrial-scale experiments. The primary objectives are to investigate the deformation patterns of the borehole pressure relief tunnel, delve into the mechanics of deep and shallow dense borehole pressure relief, uncover the mechanisms through which

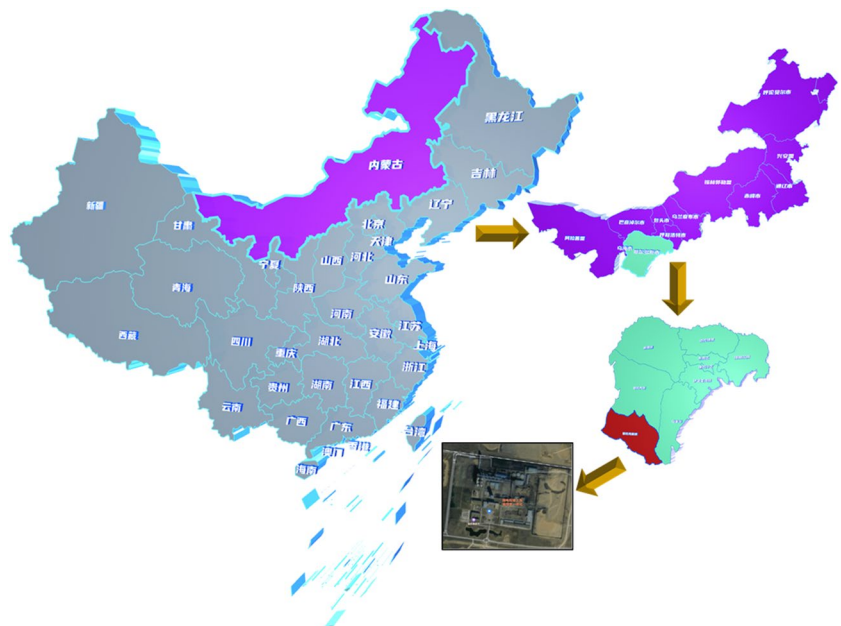
borehole parameters (such as borehole inclination and spacing), influence tunnel stability, and propose strategies for managing the deformation of the surrounding rock in deep pressure relief tunnels. The outcomes of this study serve as a theoretical foundation for the development of similar tunnel rock pressure relief techniques.

2 Engineering Background

2.1 Mine General Situation

As depicted in Fig. 1, the New Shanghai No. 1 Coal Mine is strategically located within the confines of Etuoke Front Banner, a region situated in the Inner Mongolia Autonomous Region. The mining field spans approximately 12.5 km in the north–south direction, with an east–west width ranging from 2.0 to 3.5 km, resulting in a substantial total mining field area of 39.7 km². Notably, the coal seams within this area are classified as concealed coalfields, and the geological strata exhibit dip angles ranging from 3 to 13°. At present, the predominant source of coal extraction emanates from the 1806N working face. Positioned to the north of the industrial plaza, this specific working face is demarcated by the F2 fault on its eastern boundary, serving as a pivotal waterproof protective coal pillar line. The southern region features a horizontal north wing return airway, while on the western side, one finds the 1805N working face. To the north, the F2 fault also plays a crucial role in safeguarding the coal pillars. It is important to note that both the upper and lower sections of the 1806N working face lack pre-excavated roadways and

Fig. 1 Geographical location of coal mine



are entirely devoid of goaf areas. The 1806N working face primarily targets the extraction of coal from the 8th coal seam, characterized by its structurally simplistic nature. The coal seam’s thickness varies between 3.6 and 4.25 m with an average thickness of 3.925 m and a mining height of 3.6 m. The geological orientation of the coal (rock) layer manifests a strike range between 5 and 13°, with a trend oriented between 95 and 103°. Furthermore, the dip angle of the coal seam oscillates between 1 and 7°, with an average dip angle of approximately 4°. The mining methodology employed is the inclined longwall arrangement, featuring a push–pull length of 1780 m and an inclined length spanning 382.5 m, as illustrated in Fig. 2.

2.2 Original Support Design and Deformation Characteristics of Auxiliary Roadway

In 1806N auxiliary roadway, the original design section featured a combination of straight walls and curved arches with an arched bottom. The roadway had a width of 4700 mm and a height of 3900 mm. The original support system for the roadway utilized a combination of anchor mesh (cable) spraying and reverse bottom arch anchor mesh (cable) spraying, as illustrated in Figure 3. High-strength anchor rods with a diameter of 22 mm and a length of 2800 mm were used, with anchor spacing set at 700 × 800 mm and a pre-tightening torque of 300 N·m. The anchor cables were constructed with

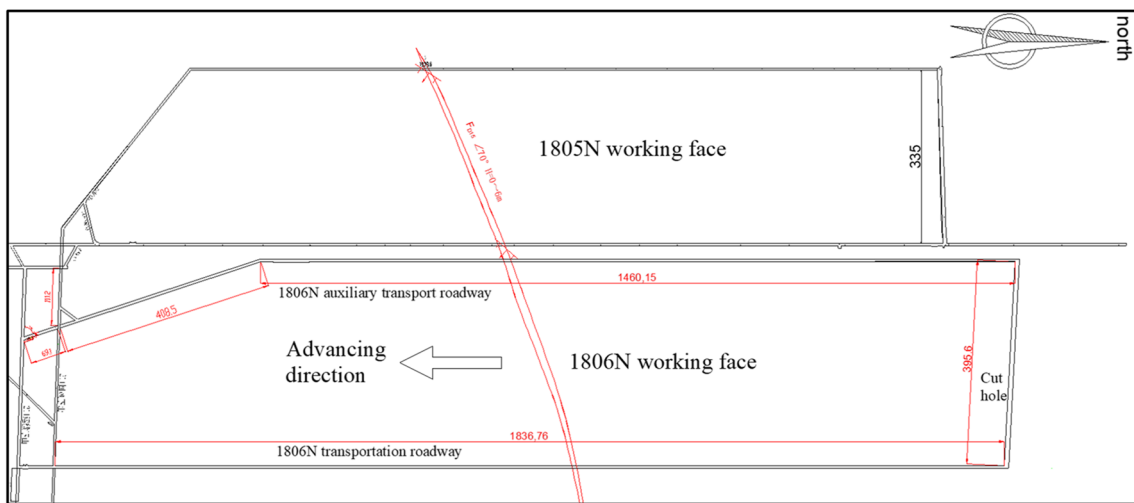
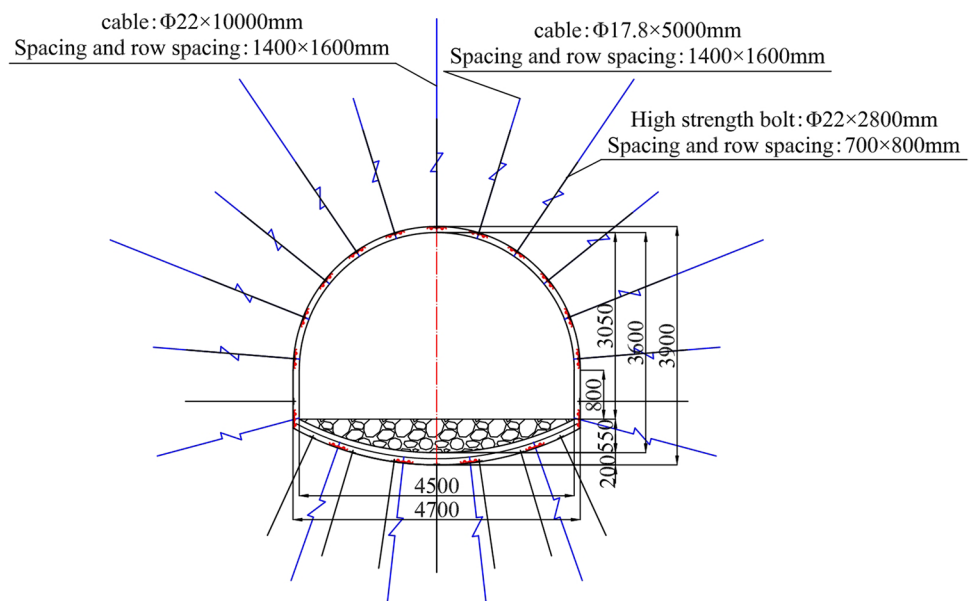


Fig. 2 1806 N working face

Fig. 3 Original support design



a 1×19 steel strand structure, featuring a diameter of 17.8 mm. The top anchor cables had a length of 10,000 mm, while the side anchor cables had a length of 5000 mm.

Despite the use of the above-mentioned support system, the roadway still experienced severe deformations, particularly during the mining phase. The primary manifestations included significant deformations of the roof and floor, with cumulative floor heaving exceeding 2 m. The failure of the roadway support structure and extensive rock deformation are depicted in Figure 4. The concrete of the roof and floor experienced widespread cracking, and numerous anchor rod cables in the roadway broke. Additionally, support components such as steel belts suffered tearing and bending failures. The entire process of roadway excavation and face mining presented a state of “advance mining followed by repairs” and “simultaneous mining and maintenance.”

3 Large Deformation Mechanism of Roadway Surrounding Rock

3.1 Physical and Mechanical Characteristics of Roadway Surrounding Rock

The distribution of rock types in the roof and floor of the 1806N coal seam is illustrated in Fig. 5. The roof is primarily composed of sandy shale and medium-grain sandstone, with localized occurrences of siltstone. The floor mainly consists of sandy shale with well-developed joint fractures.

In order to further investigate the impact of rock mechanics on the significant deformation of the roadway, mineral composition and rock mechanics parameters of the surrounding rocks in the demonstration roadway were tested and analyzed, as shown in Table 1. Additionally, the in situ stress was measured using the hollow inclusion stress relief method. The maximum horizontal principal stress was measured at 16.99 MPa, the minimum horizontal principal stress at 9.82 MPa, and the vertical stress at 11.26 MPa. The uniaxial compressive strength of the coal seam was 15.9 MPa, with ratios to the three principal stresses of 0.94, 1.62, and 1.41, respectively. The uniaxial compressive strength of the sandy shale was 17.1 MPa, with ratios of 1.0, 1.74, and 1.52 to the three principal stresses, respectively.

It was observed that the maximum principal stress exceeded the compressive strength of the coal seam and reached the compressive strength of the sandy shale. The low strength-to-stress ratio of the surrounding rocks led to rapid failure of the surrounding rocks after roadway excavation. Notably, the upper part of the roof comprised medium-grain sandstone with a high compressive strength of 61.1 MPa and ratios to the three principal stresses of 3.60, 6.22, and 5.43, with a thickness of 6.22 m. After coal mining, the roof was prone to delayed collapse, altering the movement and structural characteristics of the overlying rock layers, affecting the distribution and magnitude of stress during mining, and subsequently influencing the deformation and failure of the mined roadway.

Fig. 4 Deformation characteristics of auxiliary roadway

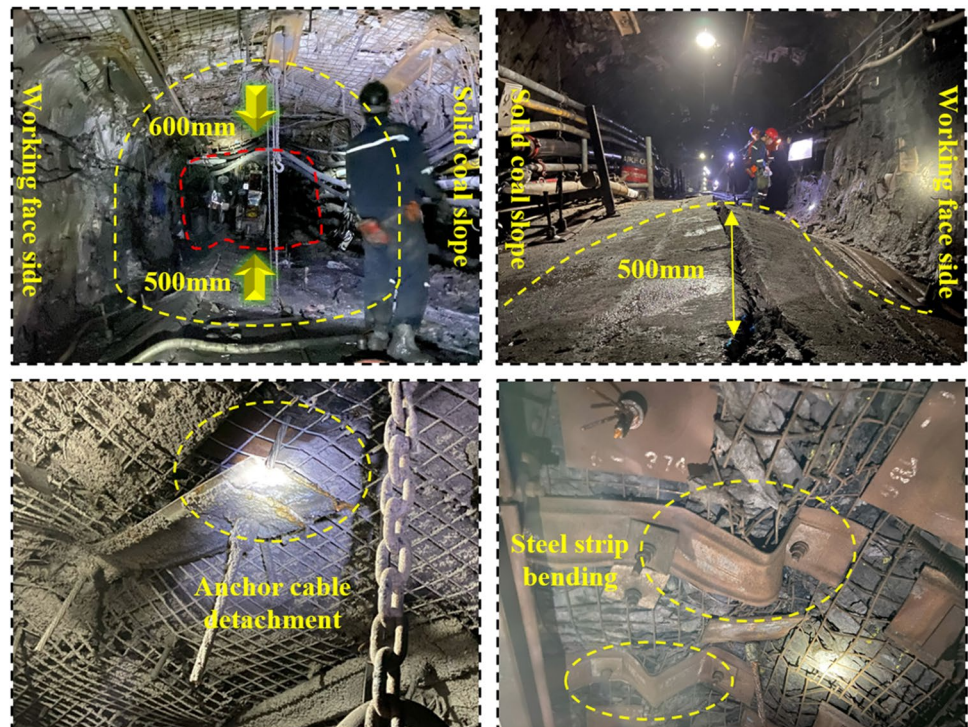


Fig. 5 Lithologic column diagram



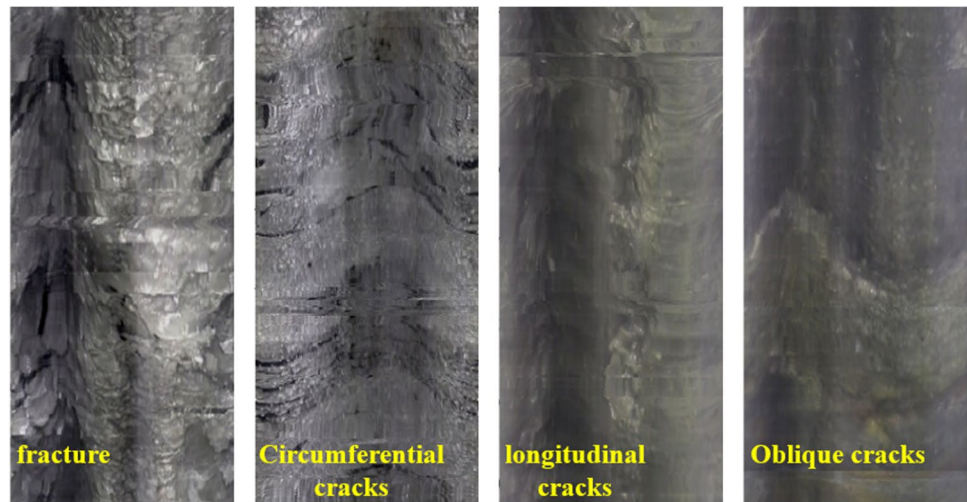
Table 1 Statistical table of mechanical properties of overlying strata on 1806N working face

Number	Rock stratum	Thickness (m)	Specific weight (kN/m ³)	Compressive strength (MPa)	Tensile strength (MPa)	Tangent modulus (GPa)	Elastic modulus (GPa)	Hard rock	Key layer
0	Coal (8)	3.6	14	15.9	0.6	5	12.5		
1	Sandy mudstone	5.15	24.8	17.1	0.7	17	42.84		
2	Medium grain sandstone	6.22	24.6	61.1	3.2	32	76.8	Hard rock	Low key stratum
3	Siltstone	2.0	22.8	20.8	0.9	14	33.6		
4	Sandy mudstone	5.68	24.8	17.1	0.7	17	42.84		
5	Fine sandstone	4.8	23.1	44.9	2.2	26	68.64	Hard rock	High key stratum
6	Sandy mudstone	3.1	24.8	17.1	0.7	17	42.84		

Furthermore, a borehole camera was used to observe the structure of the roof rock layers and investigate the impact of the integrity of the surrounding rocks on coal and rock deformation and damage, as shown in Fig. 6. The roof exhibited various bedding planes and radial, longitudinal, oblique, and composite fractures. In deep, high-stress conditions, the

extent of roadway rock failure is likely to exceed the control range of anchor support. Over time, not only does the anchoring force of the anchor bars decrease continuously but structural slippage of the anchored material occurs, leading to the extrusion of the load-bearing structure formed by the anchor bars.

Fig. 6 Types and distribution of cracks in surrounding rock



3.2 Large Deformation Mechanism of Surrounding Rock of Auxiliary Roadway

During the mining process of the working face, significant deformation and damage occurred in the auxiliary transport entryway, primarily manifesting as roof sagging and floor heaving. The analysis revealed the following mechanisms for the large deformation and damage of the surrounding rock in the auxiliary transport entryway: (1) low strength-to-stress ratio: The roof and floor of the entryway mainly consist of weakly cemented sandy mudstone, with an average uniaxial compressive strength of 14.9 MPa. The maximum principal stress in the coal mine is 16.99 MPa, resulting in a low strength-to-stress ratio of 0.88. This low ratio, coupled with highly developed joint and fracture systems, makes the entryway susceptible to damage shortly after excavation and leads to deeper rock mass failure. (2) Rock deterioration: The overlying rock contains aquifers with high water content, and the clay mineral content is substantial. Upon exposure to water, the rock undergoes sandification and mudification, significantly weakening its integrity. The excavation disturbance leads to plastic deformation, cracking, swelling, and damage in the

surrounding rock, resulting in a decrease in its strength. (3) Intense mining-induced stress: The excavation of an extremely long working face of 395.6 m exerts a strong influence on the surrounding rock, causing an increase in the extent and magnitude of mining-induced effects. Additionally, the 6.22-m-thick medium-grain sandstone overlying the coal seam has a rigid roof that is resistant to collapse. When it fractures, it releases a substantial amount of energy, leading to more pronounced dynamic loads. (4) Inappropriate tunnel layout: The maximum principal stress on the 1806N working face is oriented horizontally (with a magnitude of 16.99 MPa) and is perpendicular to the direction of the entryway layout. This represents the most unfavorable tunnel layout. (5) Support component failure: First, the support components are subject to corrosion and wear due to chemical and electrochemical factors. Second, the presence of aquifers in the surrounding rock results in the ineffectiveness of anchoring agents when they come into contact with water.

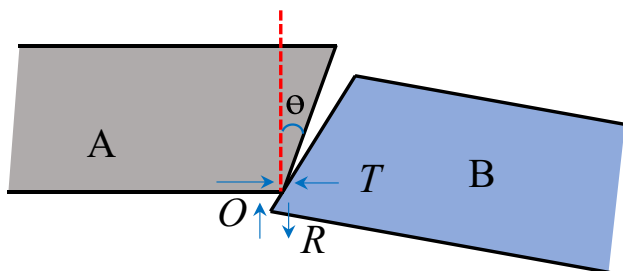


Fig. 7 Stress analysis of the basic roof broken rock block

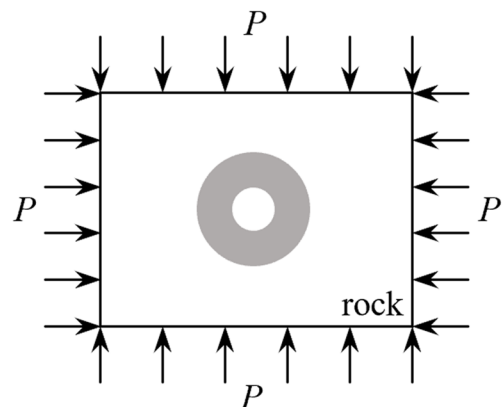


Fig. 8 Mechanical model of rock mass around borehole

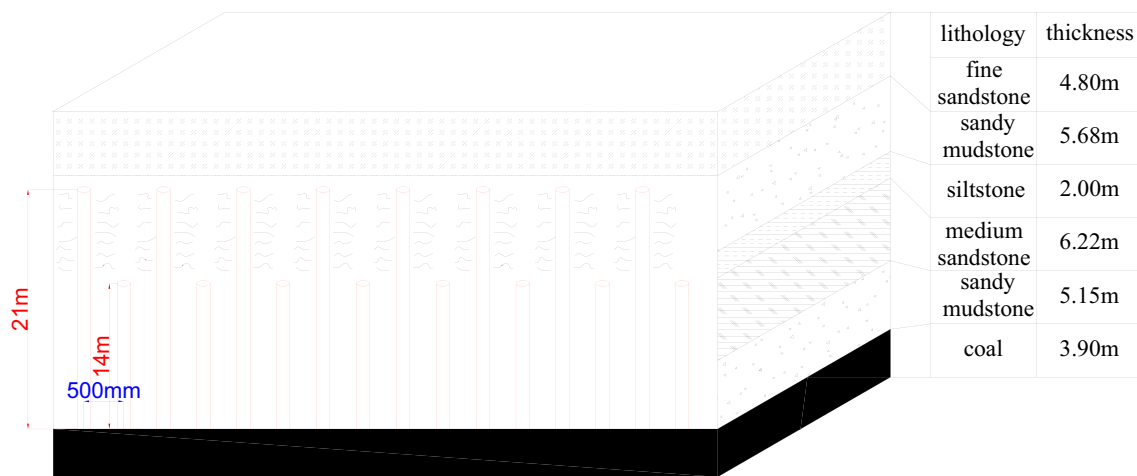


Fig. 9 Dense drilling parameters

4 Large Deformation Control of Surrounding Rock of Auxiliary Roadway

The main causes of significant deformation in the surrounding rock of the auxiliary transport roadway are soft rock, low strength-to-stress ratio, and intense mining activity. It is essential to establish stability control methods based on these three aspects. Methods to improve the mechanical properties of soft rock primarily involve strengthening anchoring. High prestress, high strength, and high toughness anchor rods/cables can effectively control discontinuous and non-coordinated expansion deformations in the surrounding rock, such as delamination, sliding, rotation, and the formation of new cracks, thereby reducing the degradation of the surrounding rock's strength [18, 19].

Improving the low strength-to-stress ratio is generally achieved by reducing the stress in the surrounding rock and increasing its strength. Regarding intense mining activity, various methods like deep-hole blasting, hydraulic fracturing, and borehole unloading are used. Among these methods, borehole unloading technology has multiple advantages and is increasingly widely applied in controlling the surrounding rock in coal mines. Therefore, the use of deep and shallow densely spaced borehole unloading is established

as a method for controlling significant deformations in the roadway. Deep boreholes sever the high-stress transfer of the upper surrounding rock, reducing stress concentration in the roof, and transferring stress to the deeper parts. Shallow boreholes fragment the surrounding rock, allowing it to promptly collapse and fill the mined-out area.

4.1 Determine the Cutting Height of the Deep Hole

After the extraction and pushing of the working face, it is assumed that the overlying n layers of rock undergo synchronous deformation to form a composite beam. According to the principles of material mechanics [20] for composite beams, the formula for calculating the load q on the overlying rock layers is derived [20].

$$(q_n)_1 = \frac{E_1 h_1^3 (\gamma_1 h_1 + \gamma_2 h_2 + \dots + \gamma_n h_n)}{E_1 h_1^3 + E_2 h_2^3 + \dots + E_n h_n^3} \tag{1}$$

In the equation: $(q_n)_1$ represents the load borne by the first layer of rock when considering the n th layer of rock, kPa; E_1, E_2, \dots, E_n are the elastic moduli of each rock layer, MPa; h_1, h_2, \dots, h_n denote the thickness of the overlying rock layers, m ; $\gamma_1, \gamma_2, \dots,$

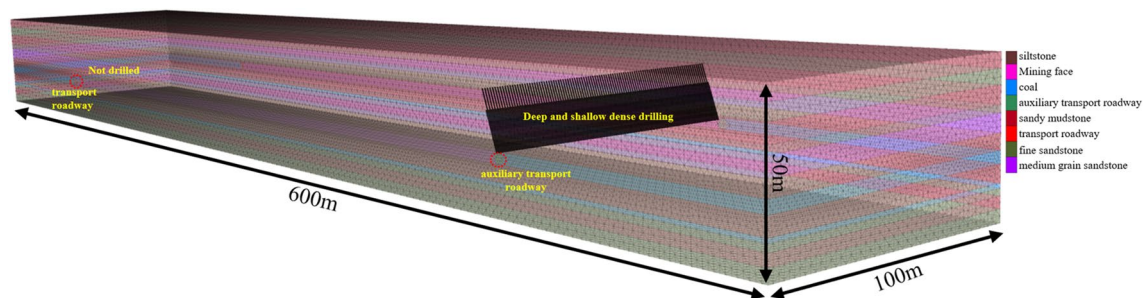


Fig. 10 Numerical model

Table 2 Physical and mechanical parameters of rock strata

Lithologic	Bulk modulus (GPa)	Shear modulus (GPa)	Cohesion (MPa)	Internal friction (°)	Tensile strength (MPa)	Density (kg·m ⁻³)
Medium sandstone	2.9	1.6	3.0	31	0.3	2550
Coal	2.7	1.4	1.2	32	0.1	1470
Sandy mudstone	5.1	3.0	3.0	29	1.1	2204
Siltstone	3.0	2.0	3.0	27	0.2	2510
Fine sandstone	43.7	27.5	3.5	31	5.3	2602

γ_n represent the respective bulk densities of the individual stratified layers, MN/m³.

The overlying rock layers are simplified based on the lithological column chart, as listed in Table 1. Substituting the parameters from the table into Eq. (1), we get: $q_1 = 127.72$ kPa, $(q_2)_1 = 67.51$ kPa, $(q_3)_1 = 77.62$ kPa, $(q_4)_1 = 84.24$ kPa, $(q_5)_1 = 84.46$ kPa, $(q_6)_1 = 92.75$ kPa. The first layer of sandy mudstone and the fifth layer of fine-grained sandstone have greater strength and thickness, exhibiting higher load-bearing capacity. Under high-intensity mining conditions, they significantly impact the management of the underlying mining field roof and the stability of the tunnel surrounding rock. Therefore, they can be regarded as low and high-level critical layers, respectively. Deep boreholes cut off the rock layers below the high-level critical layer, severing the stress transfer path. Hence, the length of the deep borehole is cut to the 4th sandy mudstone (vertical height of 19.05 m).

4.2 Determine the Cutting Height of the Shallow Hole

The design of the shallow borehole cut height should take into account both the collapse of the lower critical layer (11.37 m) and the migration characteristics of the upper rock layers. This ensures that the cut height is above the upper boundary of the most difficult-to-collapse roof and meets the filling height requirements. The overlying rock layers within the range of the cut height are assigned numerical labels, starting from the immediate roof as 1, 2, ..., up to m , with a total of m rock layers [20, 21].

$$(H_1 + H_2 + H_3 + \dots + H_m) + M - (k_1 H_1 + k_2 H_2 + k_3 H_3 + \dots + k_m H_m) = 0 \tag{2}$$

$$\sum_{i=1}^m H_i + M - k_p \cdot \sum_{i=1}^m H_i = 0 \tag{3}$$

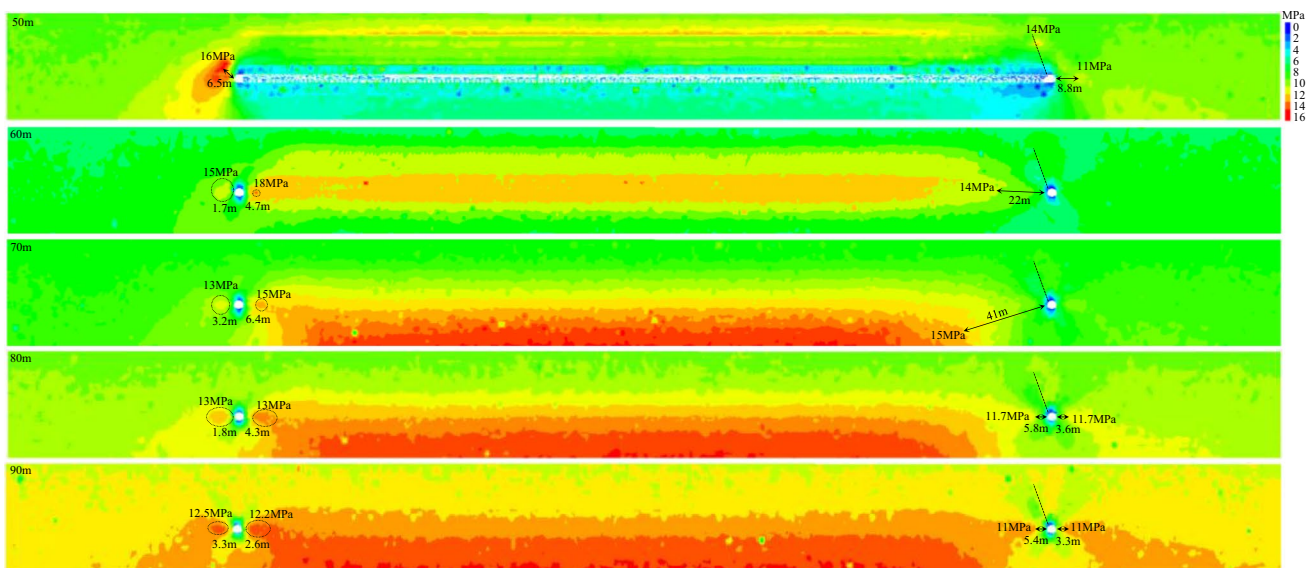


Fig. 11 Stress variation rule

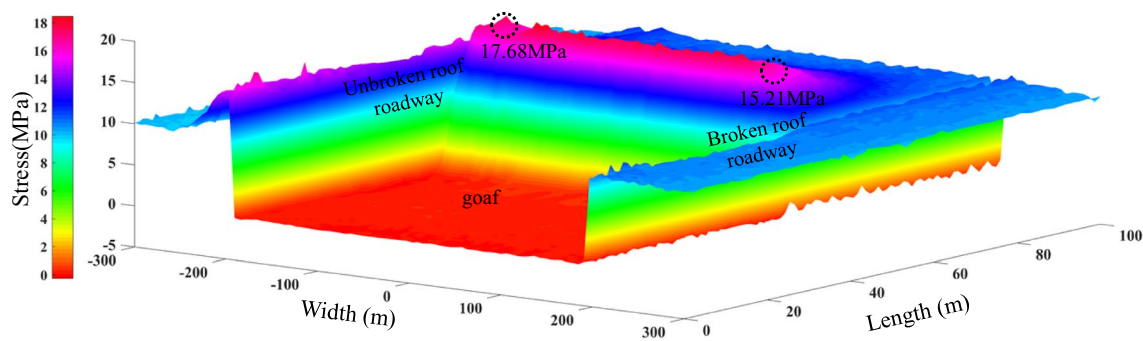


Fig. 12 Three-dimensional stress distribution of roadway roof

$$k_p = \frac{k_1 H_1 + k_2 H_2 + \dots + k_m H_m}{H_1 + H_2 + \dots + H_m} \tag{4}$$

Taking into account the potential rotational subsidence and natural collapse of the overlying rock layers, therefore...

$$h_q = \sum_{i=1}^m H_i = \frac{M}{k_p - 1} \tag{5}$$

In the equation: h_q represents the cutting height, m; M is the mining height, m. k_1, k_2, \dots, k_m represents the rock fragmentation coefficients for the roof layers of the first, second, ..., m th layer, respectively; k_p is the weighted average initial rock fragmentation coefficient, typically ranging from 1.20 to 1.40, with a chosen value of 1.28; H_1, H_2, \dots, H_m stand for the thickness of the roof layers for the first, second, ..., m th layer, respectively.

Based on the geological production conditions of the 1806N working face, a mining height of $M=3.6$ m is determined. Substituting this data yields an approximate value of $h_q=12.857$ m.

4.3 Determine the Cutting Angle

During the advancing process of the working face, lateral stresses are effectively transmitted through the masonry beam structure. The contact surface between rock blocks A and B is considered as the structural plane of the cutting roof. This severs the physical connection and stress transmission paths between the immediate roof rock blocks, ensuring the stability of the roadway surrounding rock. Based on the principles of masonry beam theory and the S-R stability theory of surrounding rock structures, a mechanical model of the fracture surface of rock blocks A and B is established, as shown in Fig. 7, and a mechanical analysis is conducted at the contact point of blocks A and B. When the shear force at the contact point is less than the frictional force, the fracture surface will not slip and become unstable. To guarantee the cutting roof effect, the shear force should exceed the frictional force [20, 21].

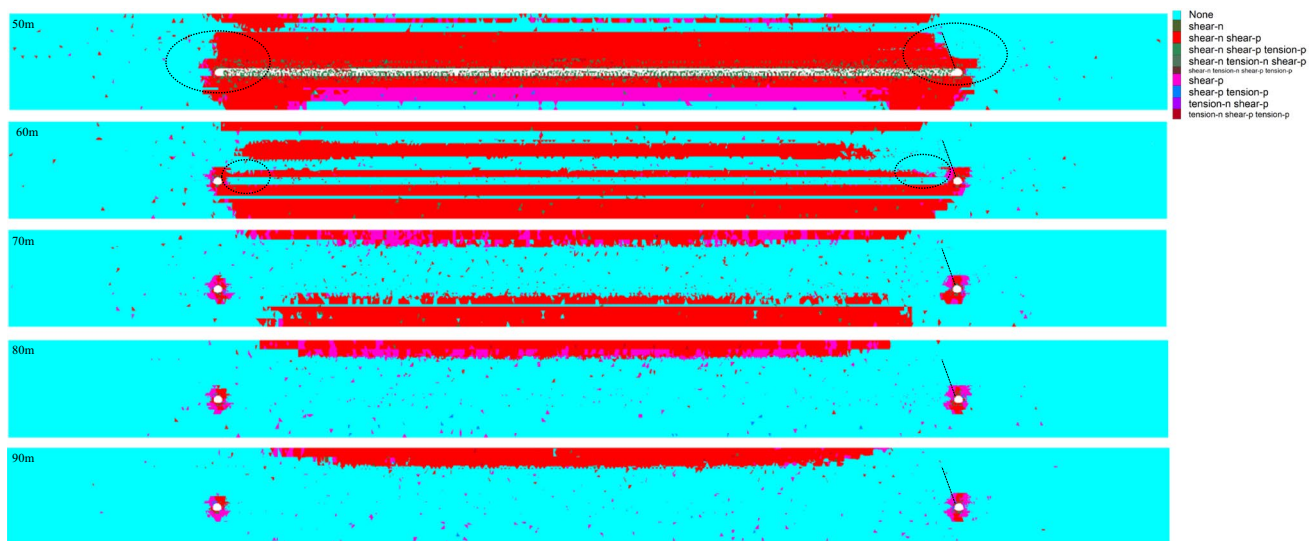
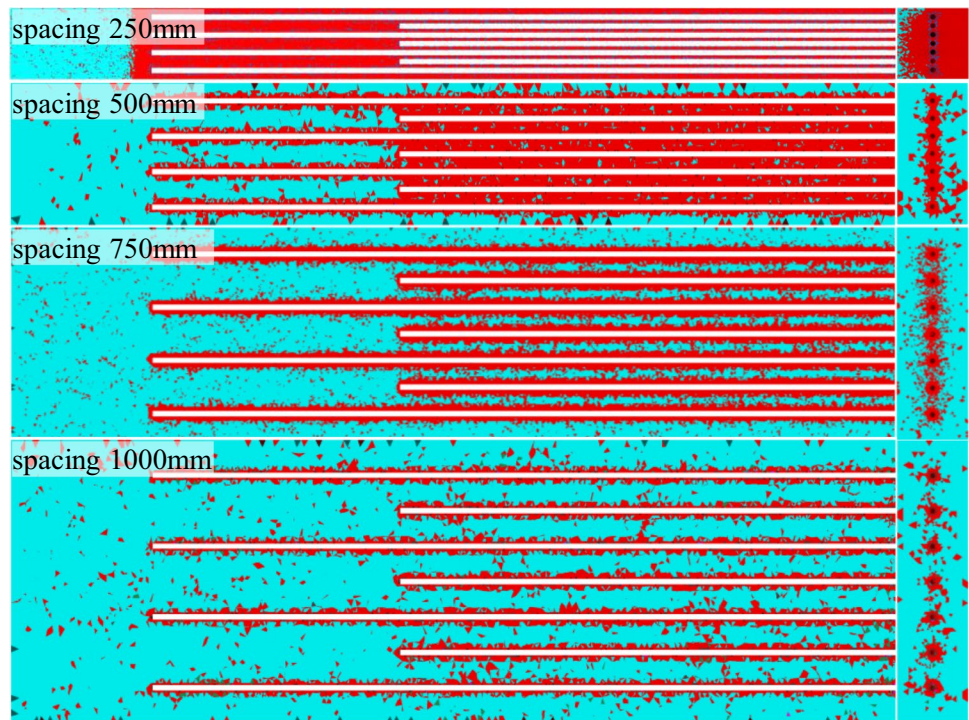


Fig. 13 Variation rule of plastic zone

Fig. 14 Variation of plastic zone with different hole spacing



The stability criteria for rock block B are as follows:

$$(T\cos\theta - R\sin\theta)\tan\varphi \geq R\cos\theta + T\sin\theta \quad (6)$$

The conditions for the instability and sliding of rock block B are as follows:

$$(T\cos\theta - R\sin\theta)\tan\varphi \leq R\cos\theta + T\sin\theta \quad (7)$$

Simplifying the equation yields:

$$T\sin(\varphi - \theta) \leq R\cos(\varphi - \theta) \quad (8)$$

$$\frac{R}{T} \geq \tan(\varphi - \theta) \quad (9)$$

$$\theta \geq \varphi - \arctan\frac{R}{T} \quad (10)$$

$$T = \frac{qL^2}{2(h - \Delta s)} \quad (11)$$

$$\theta \geq \varphi - \arctan\frac{2(h - \Delta s)}{L} \quad (12)$$

Increasing the cutting angle will intensify the lateral cantilever additional stress. To ensure the smooth collapse of the immediate roof rock block, the cutting angle should be minimized as much as possible.

$$\theta = \varphi - \arctan\frac{2(h - \Delta s)}{L} \quad (13)$$

In the equation, θ represents the cutting angle of the roof, degree; Δs denotes the subsidence of rock block B, m; L stands for the lateral fracture span of the immediate roof, m; φ represents the internal friction angle of the immediate roof, degree; h signifies the thickness of the immediate roof stratum, m.

According to the engineering geological conditions of the 1806N working face and the aforementioned calculation results, with $\varphi = 34^\circ$, $L = 21.26$ m, $\Delta s = 2.5$ m, and $h = 5.15$ m, substituting into the equation yields $\theta = 20^\circ$.

4.4 Determine Hole Spacing

Following the excavation of boreholes, we assume that the surrounding rock is in an elastic state, and given that the length of the borehole is significantly greater than its diameter, we analyze it as a two-dimensional strain problem. The vertical and horizontal stresses acting on the borehole are both simplified as uniform stresses, forming a mechanical model for the borehole and the surrounding rock, as depicted in Fig. 8. By applying elastic theory, we determine the stress state of the rock mass around the borehole. Based on plasticity conditions, we evaluate whether the rock mass undergoes yielding, resulting in the approximate boundary equation for the plastic zone around the borehole, which is also referred to as the destressing zone [20, 21].

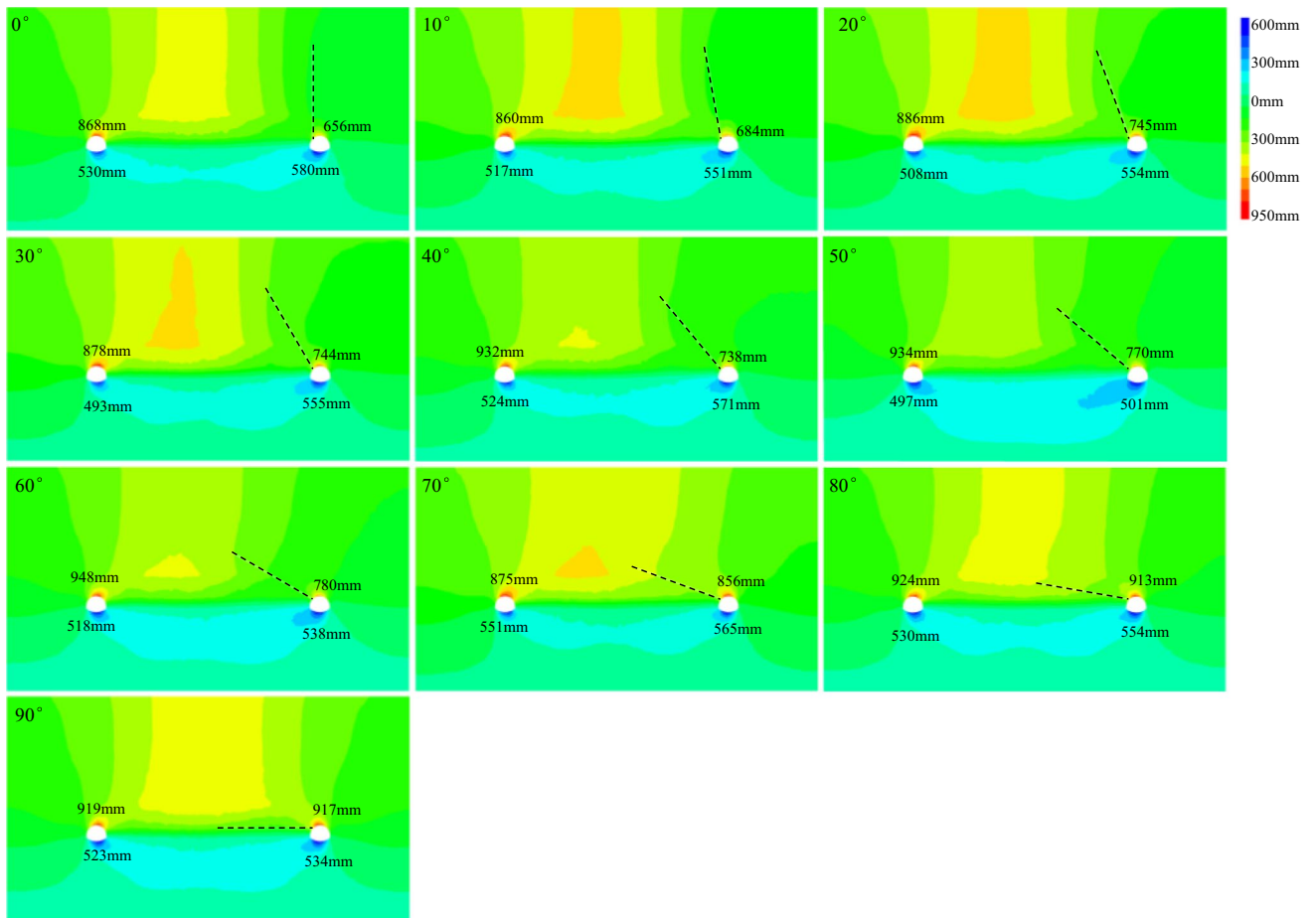
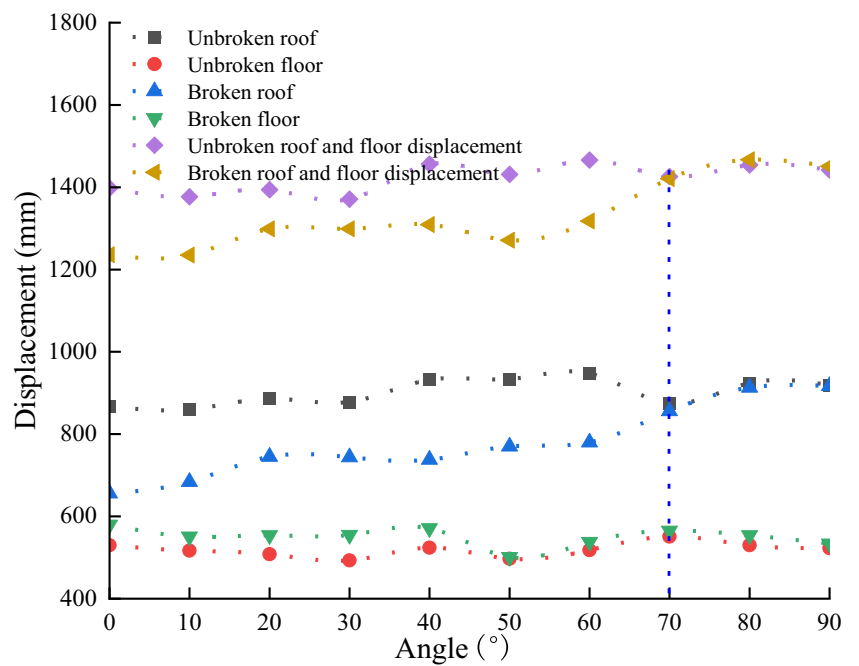


Fig. 15 Displacement cloud image of different drilling angles

Fig. 16 Displacement variation rule of different drilling angles



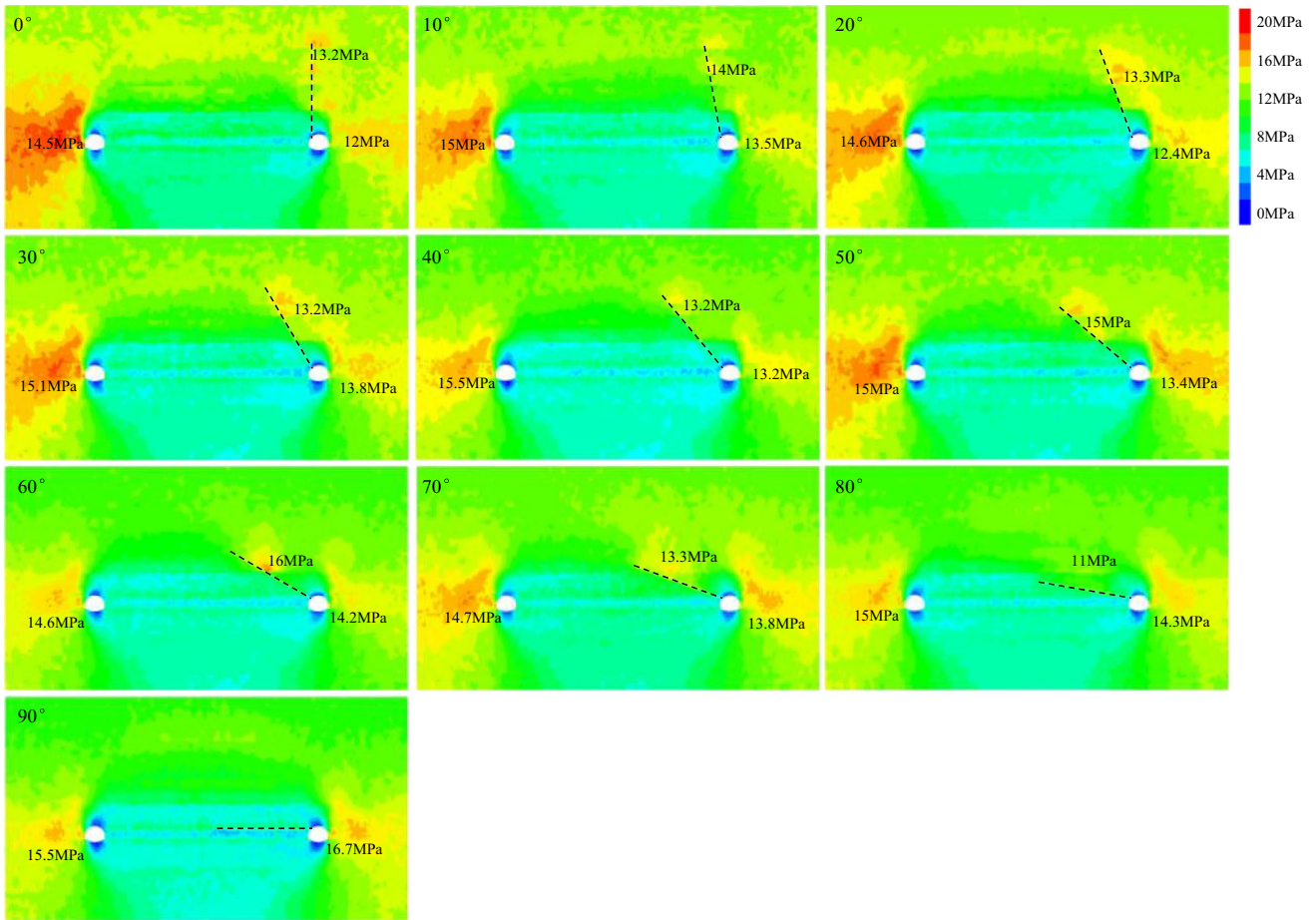
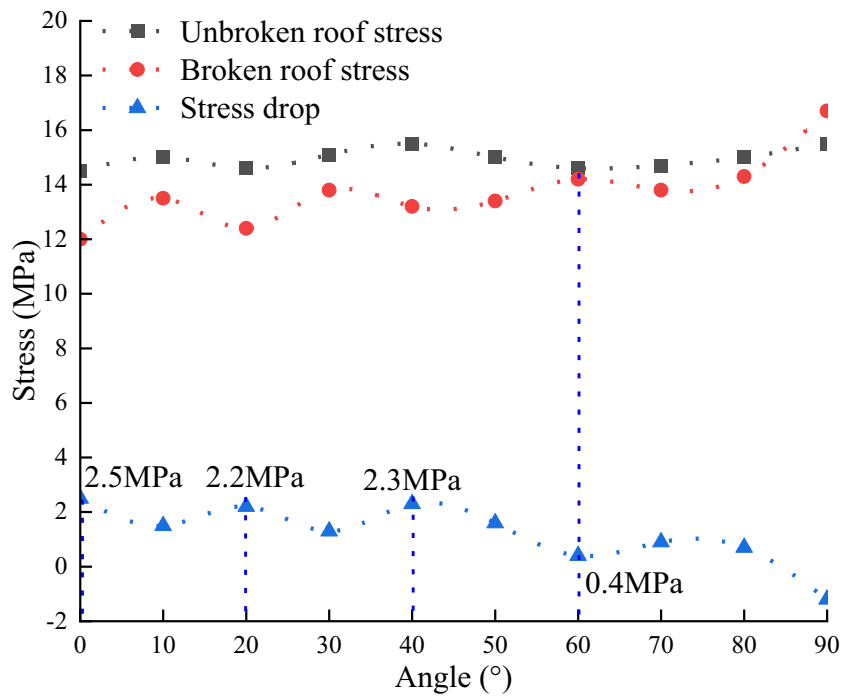


Fig. 17 Stress nephogram of different borehole angles

Fig. 18 Stress variation rule of different drilling angles



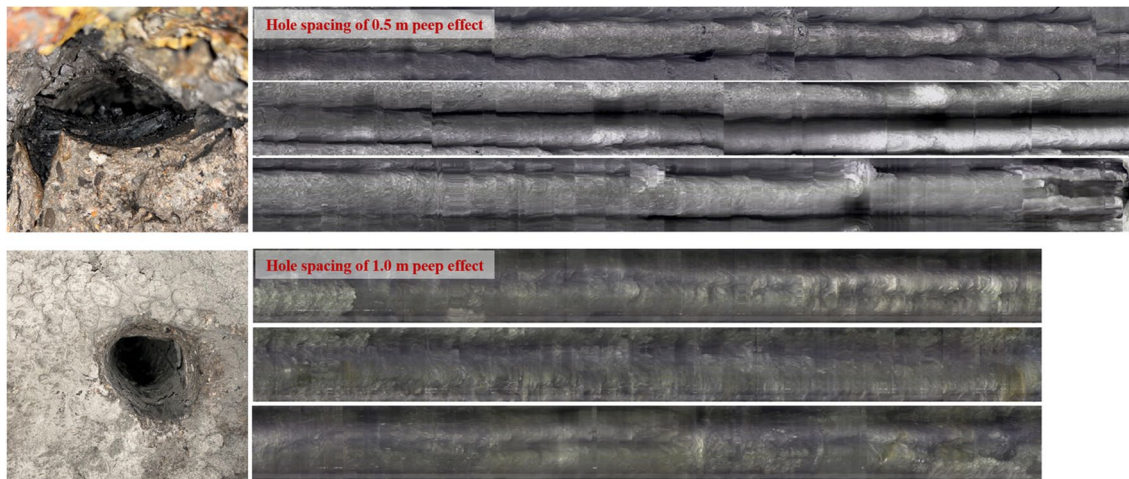


Fig. 19 Different hole spacing drilling peep

$$\rho = \frac{ap}{C\cos\zeta - p\sin\zeta} \tag{14}$$

In the equation, ρ represents the polar coordinate at any point around the borehole; a denotes the borehole diameter, m; c stands for the cohesion of the surrounding rock, MPa; ζ represents the internal friction angle of the surrounding rock, degree; p signifies the horizontal stress acting on the borehole, MPa.

According to geological and production conditions of the 1806N working face, as well as observed mining pressure data, where $a = 0.075$ m, $c = 3.5$ MPa (as the roof rock layers primarily consist of mudstone and sandstone), $\zeta = 34^\circ$, $p = 3.5$ MPa, we solve for $\rho = 0.32$ m. Thus, the close borehole spacing between boreholes, denoted as “ d ,” is calculated as $d = 2\rho \times 0.8$, resulting in $d = 0.512$ m, which is approximated to 0.5 m.

4.5 Deep and Shallow Dense Drilling Parameter Design

Based on the calculations of the vertical height and cutting angle for deep and shallow boreholes mentioned above,

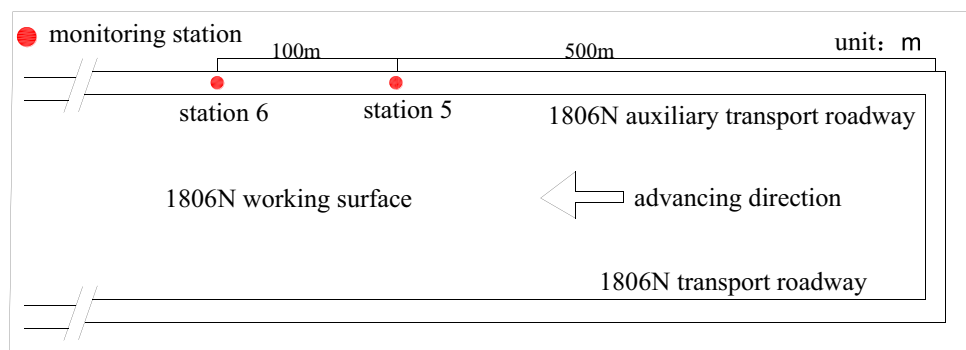
the final determination of the lengths for deep and shallow closely spaced boreholes is made. The vertical heights for deep and shallow boreholes are 19.05 m and 12.857 m, respectively, with a cutting angle of 20° . Consequently, the depths of the deep and shallow boreholes are 20.27 m and 13.68 m, respectively. For the sake of construction convenience, the depths chosen are 21 m for the deep boreholes, 14m for the shallow boreholes, with a cutting angle of 20° , and a spacing of 0.5 m, as illustrated in Fig. 9.

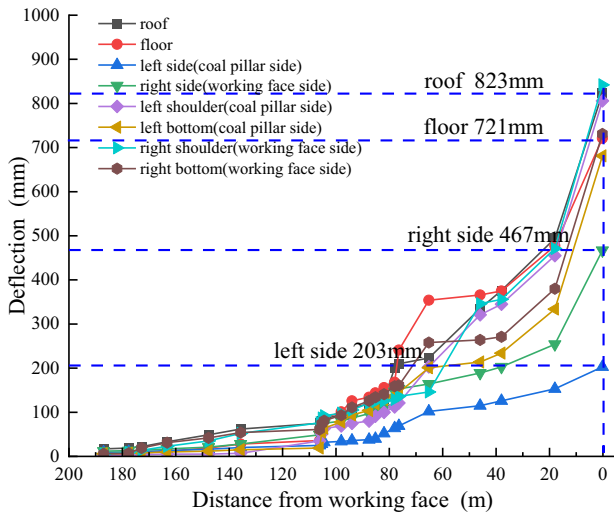
5 Numerical Calculation of Deep and Shallow Dense Drilling

5.1 Field Numerical Model

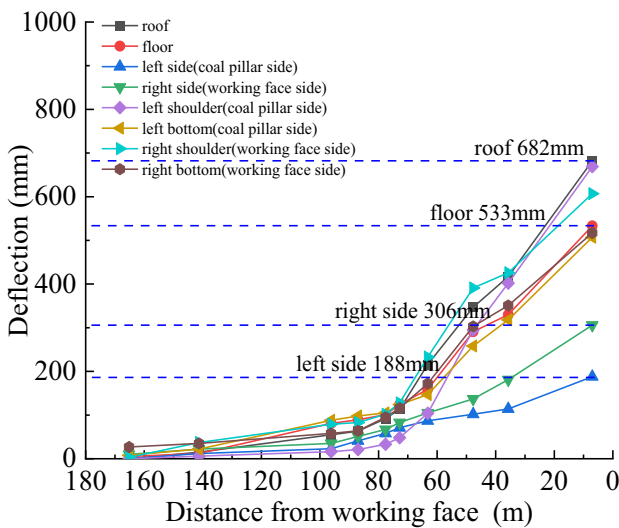
A model was constructed for the 1806N working face with dimensions of 600 m in length, 100 m in width, and 50 m in height, yielding a total of 8,314,329 individual elements. The stratigraphic divisions were based on the surrounding rock types, and the failure criterion for the model was established using the Mohr–Coulomb criterion. On the left side of the roadway, no deep or shallow closely spaced boreholes

Fig. 20 Layout of deformation measuring station of surrounding rock





Station 6 displacement monitoring



Station 5 displacement monitoring

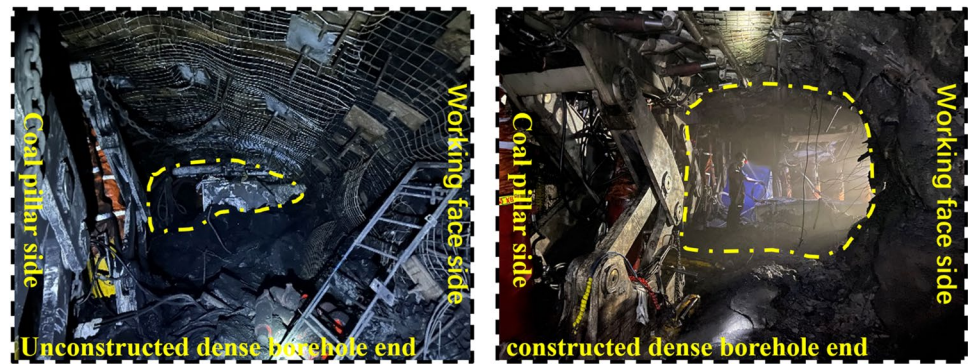
Fig. 21 Deformation curves of roadway surrounding rock at stations 5 and 6

were implemented. Conversely, on the right side, closely spaced boreholes were drilled with specific parameters: a cutting angle of 20 degrees, shallow borehole depth set at 14 m, deep borehole depth at 21 m, and a spacing of 500 mm. Following the on-site construction sequence, the excavation commenced with the development of both the left and right roadways. Subsequently, the excavation of closely spaced boreholes was carried out. In line with the on-site mining progression, coal seam extraction proceeded incrementally, with each cycle advancing by 10 m. This process was repeated ten times. The model’s configuration is illustrated in Fig. 10, and detailed mechanical parameters can be found in Table 2.

As shown in Fig. 11, a stress analysis of the surrounding rock was conducted after the working face had advanced 50 m. No intensive drilling was carried out in the transport drift, while intensive drilling was implemented in the auxiliary transport drift. At the 50-m face of coal seam excavation, stress concentrations were observed 6.5 m from the transportation drift, with the maximum stress reaching 16 MPa. Similarly, stress concentrations were present at a distance of 8.8 m from the auxiliary transportation drift, with the maximum stress recorded at 11 MPa. At the 10-m advance of the working face, stress concentrations were observed at distances of 1.7 m to the left and 4.7 m to the right of the transportation drift, with stress levels reaching 15 MPa and 18 MPa, respectively. Additionally, stress concentrations were detected at a distance of 22 m to the left of the auxiliary transportation drift, with the maximum stress recorded at 14 MPa. At the 20-m advance of the working face, stress concentrations were noted at distances of 3.2 m to the left and 6.4 m to the right of the transportation drift, with stress levels of 13 MPa and 15 MPa, respectively. Moreover, stress concentrations were found at a distance of 41 m to the left of the auxiliary transportation drift, with the maximum stress reaching 15 MPa. At the 30-m advance of the working face, stress concentrations were observed at distances of 1.8 m to the left and 4.3 m to the right of the transportation drift, both registering at 13 MPa. Additionally, stress concentrations were present at a distance of 5.8 m to the left and 3.6 m to the right of the auxiliary transportation drift, with a maximum stress of 11.7 MPa in both cases. At the 40-m advance of the working face, stress concentrations were found at distances of 3.3 m to the left and 2.6 m to the right of the transportation drift, with stress levels of 12.5 MPa and 12.2 MPa, respectively. Furthermore, stress concentrations were detected at a distance of 5.4 m to the left and 3.3 m to the right of the auxiliary transportation drift, with the maximum stress in both cases reaching 11 MPa. The stress distribution in the tunnel roof is illustrated in Fig. 12. After the dense borehole construction in the auxiliary transportation drift, a significant reduction in stress concentration in the tunnel was observed.

In accordance with Fig. 13, a plastic zone is observed to develop near the transportation drift face. The construction of dense boreholes in the auxiliary transportation drift disrupts the distribution of the plastic zone, resulting in a smaller plastic zone area in comparison to the area near the transportation drift. At the 10-m advance of the working face, the presence of dense boreholes in the auxiliary transportation drift serves to curtail the development of the plastic zone. Nevertheless, at advances of 20 m, 30 m, and 40 m, the construction of dense boreholes in the auxiliary transportation drift causes a degree of damage, leading to a

Fig. 22 Deformation effect of roadway end



slightly larger plastic zone area near the auxiliary transportation drift as opposed to the transportation drift.

5.2 Research on Key Parameters of Dense Drilling

5.2.1 Plastic Zone Distribution with Different Hole Spacing

To analyze the impact of different borehole spacing on the behavior of shallow and deep dense boreholes, numerical simulations were conducted, which align with the actual site conditions. The model borehole spacings were set at 0.25 m, 0.5 m, 0.75 m, and 1.0 m, with shallow boreholes having a length of 14 m and deep boreholes measuring 21 m, as illustrated in Fig. 14. At a spacing of 0.25 m, a highly developed plastic zone is observed between shallow and deep boreholes, with complete interconnection of the plastic zone between deep boreholes. At a spacing of 0.5 m, the plastic zone between shallow boreholes interconnects, effectively fracturing the surrounding rock in the shallow region. However, the plastic zone between deep boreholes does not interconnect, serving to maintain the stability of the deep surrounding rock. At a spacing of 0.75 m and 1.0 m, the plastic zone between shallow and deep boreholes does not fully interconnect.

5.2.2 Numerical Simulation of Different Borehole Angles

In order to investigate the impact of borehole angles on the relief effect, a numerical analysis with varying borehole angles was conducted, focusing on deformation and stress analysis at the working face. As shown in Figs. 15 and 16, displacement maps and their trends under different borehole angles were observed. It was evident that after roof cutting, the displacement of the roof significantly reduced, while the floor displacement was slightly greater. With an increase in borehole angle, the roof deformation exhibited a general increasing trend, while floor deformation continuously decreased. For borehole angles between 0 and 20°, the displacement of the roof and floor after roof cutting was relatively small. However, when borehole angles exceeded 70°, the displacement of the roof and floor after

roof cutting exceeded that of the unreinforced roof and floor, as shown in Figs. 15 and 16. As depicted in Figs. 17 and 18, stress maps and their trends under different borehole angles were examined. When borehole angles were less than 80°, the stresses after roof cutting were all lower than those without roof cutting. At borehole angles of 0° and 20°, the stress in the roadway sides was less than 12.5 MPa, while at other borehole angles, the stress exceeded 13 MPa. Stress differences exceeded 2 MPa at borehole angles of 0°, 20°, and 40°. A comprehensive analysis suggests that borehole angles less than 20° result in better stress relief.

6 Engineering Application

6.1 Deformation Characteristics of Drilling with Different Hole Spacing

On-site dense borehole construction with different borehole spacings was carried out, considering borehole spacings of 1000 mm and 500 mm, and the results are shown in Fig. 19. When the borehole spacing is 500 mm, the boreholes exhibit a pronounced fracturing and relief effect, with a fracture rate inside the boreholes reaching 80%. In contrast, when the borehole spacing is 1000 mm, the boreholes undergo flattening deformation, and the rate of fracture occurrence inside the boreholes is low, with shallow cracks.

6.2 Field Test and Monitoring Design

With deep and shallow dense borehole pressure relief as the technical foundation, the research team has proposed a method suitable for controlling significant deformations in soft rock. In accordance with the on-site support design, field tests involving deep and shallow dense boreholes for roof cutting were conducted to validate their effectiveness in supporting substantial rock deformations. To comprehensively analyze the control effects of deep and shallow dense boreholes on tunnel surrounding rock, monitoring stations

5 and 6 were established. The grid point method was used for deformation monitoring across the entire cross-section of the tunnel. The specific layout of monitoring stations is illustrated in Fig. 20.

Monitoring station 5 is located in the section where dense borehole construction takes place, while monitoring station 6 is situated outside this dense borehole construction zone. Analysis of the deformation curves from monitoring stations 5 and 6 reveals that the deformation of the surrounding rock decreases after roof cutting. The cumulative deformation of the roof decreased from 823 to 682 mm, and the floor's cumulative deformation decreased from 721 to 533 mm. The cumulative deformation of the left wall decreased from 203 to 188 mm, and the right wall's cumulative deformation decreased from 467 to 306 mm. The deformation of the roof, floor, left wall, and right wall decreased by 17.13%, 26.07%, 7.4%, and 34.48%, respectively. After the dense borehole construction at the end of the auxiliary transport roadway (1806 N), noticeable reductions in deformation were observed, as depicted in Figs. 21 and 22.

7 Conclusion

- To address the significant deformation issues, such as floor heave and roof sag, encountered during the excavation of the auxiliary transport roadway in the working face, we have analyzed the deformation failure mechanisms as follows: (a) Low strength-to-stress ratio: The low strength-to-stress ratio, along with extensive joint fractures, makes the roadway prone to damage and propagation into the surrounding rock post-excavation. (2) Rock deterioration: Water-induced sanding and silting of the surrounding rock. Plastic deformation during excavation, leading to strength degradation. (3) High mining-induced stress: Rapid working face excavation generates intense dynamic stress, compromising rock stability. (4) Inadequate roadway layout: roadway orientation relative to the maximum horizontal principal stress affects stability. (5) Support material failure: Corrosion, damage to support components, and anchor agent failure upon water exposure.
- Combining deep and shallow dense borehole drilling effectively controls roof fracturing and mitigates tunnel deformations. Deep boreholes reduce stress concentration, while shallow ones promote timely roof collapse and cavity filling. The approach, supported by theoretical analysis, recommends optimal parameters: 21 m length for deep boreholes, 14 m for shallow ones, both at a 20° angle, and spaced 0.5 m apart, meeting design requirements.
- We developed a numerical model to simulate densely spaced borehole roof fracturing in tunnels, accurately replicating the tunnel's damage evolution process. The findings are as follows: (1) After roof fracturing, stress concentration in the tunnel's surrounding rock decreased, extending deeper into the rock mass. At the tunnel ends, deformations significantly reduced, and the development of the plastic zone was severed. (2) A 0.25-m borehole spacing caused excessive plastic zone development, damaging the surrounding rock. Spacings of 0.75 m and 1.0 m lacked effective connectivity between deep and shallow borehole plastic zones, resulting in ineffective roof fracturing. However, a 0.5-m spacing efficiently connected plastic zones, ensuring successful roof fracturing. (3) Angles below 20° caused minimal roof and floor deformations post-fracturing, while those exceeding 70° led to increased deformations compared to non-fractured scenarios. At 0° and 20°, tunnel edge stress remained under 12.5 MPa, while other angles surpassed 13 MPa. In essence, the unloading effect was stronger with angles below 20°.
- Through on-site experiments and engineering applications, the practicality of densely spaced boreholes, both deep and shallow, has been confirmed. This approach effectively manages substantial deformations in soft rock formations, making it a valuable reference for stability control in similar soft rock tunnels.

Data Availability Data is available upon request.

References

- Ram S, Waclawik P, Nemcik J et al (2023) Mechanical behaviors of deep pillar sandwiched between strong and weak layers. *J Rock Mech Geotech Eng* 15(5):1111–1126
- Ibrahim B, Ahenkorah I, Ewusi A (2022) Explainable risk assessment of rock bolts' failure in underground coal mines based on categorical gradient boosting and Shapley additive explanations (SHAP). *Sustainability* 14(19):11843
- Vardar O, Wei C, Zhang C et al (2022) Numerical investigation of impacts of geological faults on coal burst proneness during roadway excavation. *Bull Eng Geol Env* 81:1–12
- Małkowski P (2015) The impact of the physical model selection and rock mass stratification on the results of numerical calculations of the state of rock mass deformation around the roadways. *Tunn Undergr Space Technol* 50:365–375
- Huang X, Guo J, Miao Y et al (2023) A study on the roof-cutting and pressure releasing technology of roof blasting. *Appl Sci* 13(17):9968
- Hu L, Zhang Y, Huang Z et al (2023) Coal-rock dynamic disaster prevention mechanism based on the dual loads of dynamic barrier and static pressure relief by hydraulic slotting. *ACS Omega* 8(8):7639–7647
- Yin Y, Chen B, Zhang Y et al (2024) Experimental study and evaluation on the weakening of bursting liability of coal with boreholes. *Eng Fail Anal* 155:107754

8. Hu C, Wang E, Li Q et al (2022) Research on the Key Technology of gob-side entry retaining by roof cutting for thick and hard sandstone roofs. *Sustainability* 14(16):9941
9. Yan LU, Xizheng ZOU, Changyou LIU et al (2006) Technology of digging stress-relax entry by the roadside and its application. *J Mining Safe Eng* 23(3):329–332
10. Luofeng W, Fuxing J, Zhengxing Y (2009) Similar material simulation experiment on destressing effects of the deep thick coal seam with high burst liability after mining upper and lower protective seams. *Chinese J Geotech Eng* 31(3):442–446
11. Enbing YI, Zonglong MU, Linming DOU et al (2011) Study on comparison and analysis on pressure releasing effect of boreholes in soft and hard seam. *Coal Sci Technol* 39(6):1–5
12. Honggang LIU, Yongnian HE, Jinhai XU et al (2007) Numerical simulation and industrial test of boreholes distressing technology in deep coal tunnel. *J China Coal Soc* 32(1):33–37
13. Zhang S, Li Y, Shen B, Sun X, Gao L et al (2019) Effective evaluation of pressure relief drilling for reducing rock bursts and its application in underground coal mines. *Int J Rock Mech Mining Sci* 114:7–16
14. Chuan-yang JI, Yu-jing JI, Xue-peng ZH et al (2017) Laboratory and numerical experiments on pressure relief mechanism of large-diameter boreholes. *Chinese J Geotech Eng* 39(6):1115–1122
15. Meng W, Xiangyu W, Tongqiang X (2017) Borehole destressing mechanism and determination method of its key parameters in deep roadway. *J China Coal Soc* 42(5):1138–1145
16. Huabo L, Yixin Z, Yaodong J et al (2018) Pressure relief and disaster prevention technology by large diameter borehole in fully mechanized caving face. *Safe Coal Mines* 49(05):79–82. <https://doi.org/10.13347/j.cnki.mkaq.2018.05.020>
17. Decheng G, Dong L, Fuxing J et al (2020) Reasonable pressure-relief borehole spacing in coal of different strength. *J Mining Safe Eng* 37(03):578–585. <https://doi.org/10.13545/j.cnki.jmse.2020.03.017>
18. Tian M, Gao X, Zhang A et al (2024) Study on the deformation failure mechanism and coupling support technology of soft rock roadways in strong wind oxidation zones. *Eng Fail Anal* 156:107840
19. Zhu Q, Li T, Gao X et al (2023) Deformation characteristics and failure evolution in deep high-stress roadways under creep action. *Eng Fail Anal* 154:107689
20. Qiangling Y, Furong W, Shoulong Ma et al (2022) Characteristics and control of strong underground pressure appear under irregular section normal fault roadway pillar. *J Mining Safe Eng* 39(06):1095–1107. <https://doi.org/10.13545/j.cnki.jmse.2021.0700>
21. Shangyuan C, Fei Z, Hongjian W et al (2019) Determination of key parameters of gob-side entry retaining by cutting roof and its application to a deep mine. *Rock Soil Mech* 40(01):332–342. <https://doi.org/10.16285/j.rsm.2017.2194>

Publisher's Note Springer Nature remains neutral with regard to jurisdictional claims in published maps and institutional affiliations.

Springer Nature or its licensor (e.g. a society or other partner) holds exclusive rights to this article under a publishing agreement with the author(s) or other rightsholder(s); author self-archiving of the accepted manuscript version of this article is solely governed by the terms of such publishing agreement and applicable law.